

An Ultra-Compact and Reproducible Fiber Tip Michelson Interferometer for High-Temperature Sensing

Xun Wu¹, Shengnan Wu^{1, 2, *}, Xiaolu Chen³,
Huaguan Lin¹, Erik Forsberg¹, and Sailing He^{1, 4, *}

(Invited Paper)

Abstract—An ultra-compact fiber tip Michelson interferometer (MI), primarily aimed for a reproducible and stable high-temperature sensing probe is developed and demonstrated. Both single-mode fiber (SMF) and polarization maintaining fiber (PMF) are considered and compared. The tip MI is fabricated by only using a one-step partial-polishing technique, which forms a half oblique and half vertical end face and functions as a beam splitter. A wide spectra analysis proved that the interferometer has an optical path difference (OPD) that is consistent across samples. When the lead-in fiber suffers from bending or twisting, the interference spectrum for the PMF case is more stable than that for the SMF case. Experimental results show a linear average temperature sensitivity of 15.15 pm/°C in the range of 100°C to 1000°C for three tested PMF samples, and the difference between the sensitivities of the samples is less than 4.0%. The ease of fabrication, highly compact structure, reproducibility, and excellent resistance to mechanical disturbance performance suggest that the proposed PMF tip MI is highly promising as a high temperature sensing probe with high spatial resolution.

1. INTRODUCTION

Fiber interferometers are a class of devices of considerable interest for a wide range of sensing applications due to their compactness, ease of fabrication, and convenient operation. Various methods to fabricate fiber interferometers sensors have been reported [1–3]. Of special interest are the Fabry-Perot (FP) interferometers, which have many advantages such as high resolution and wide wavelength operation range. Splicing a conventional single mode fiber (SMF) and a section of photonic crystal fiber (PCF) together can form a micro-cavity at the splice joint [4, 5]. Liu et al. [6] formed an optical fiber Fabry-Perot relative humidity sensor by splicing a short section of hollow-core photonic crystal fiber (HCPCF) to single mode fiber and covering chitosan film at the end of HCPCF that shows good stability and fast response time less than 1 min. Su et al. [7] built an FP interferometer by splicing a suspended-core optical fiber (SCF) to the single-mode fiber for high-temperature sensing. The temperature sensitivity was 12.51 pm/°C over the temperature range of 50–800°C. Relying on simple cleaving and splicing, optical fiber fused splicing technology is quite easy and reliable. The fiber tip FP interferometers made by fiber cleaving and splicing technology are frequently reported for high-temperature measurement [8–12]. This is a simple and low-cost method to fabricate an FP interferometer or other types of sensors such as Mach-Zehnder interferometer [13]; however, it suffers from low reproducibility since the length

Received 27 October 2021, Accepted 31 December 2021, Scheduled 13 January 2022

Invited paper for the Commemorative Collection on the 150-Year Anniversary of Maxwell's Equations.

* Corresponding author: Shengnan Wu (wushengnan@zju.edu.cn), Sailing He (sailing@zju.edu.cn).

¹ Centre for Optical and Electromagnetic Research, State Key Laboratory of Modern Optical Instrumentation, Zhejiang Provincial Key Laboratory for Sensing Technologies, Zhejiang University, Hangzhou 310058, China. ² Ningbo Research Institute, Zhejiang University, Ningbo 315100, China. ³ South China Academy of Advanced Optoelectronics, South China Normal University, Guangzhou 510006, China. ⁴ Shanghai Institute for Advanced Study of Zhejiang University, China.

of the FP cavity cannot be accurately controlled, which means that each sensor produced needs to be calibrated separately before it can be used for sensing purposes. Femtosecond laser pulses with extremely high peak power have been successfully used to directly write FP structures [14–16], a high-precision method which is effective and reproducible. The same technique has also been used to fabricate a fiber tip Michelson interferometer (MI) sensor that operates in a reflection mode for detection and that exhibits high refractive index (RI) sensitivity [17]. They etched off part of the fiber core, then coated the end face with silver film to enhance the reflectivity, forming the MI fiber tip interferometer with an open micro-cavity used as the RI sensor, which exhibits a compact sensor head, good mechanical reliability, wide operation range, and high sensitivity of 975 nm/RI unit at an RI value of 1.484. However, fabrication using a femtosecond laser is typically prohibitively costly for most practical applications.

Angled fibers fabricated by end-polishing techniques have been widely used to implement fiber interferometer sensors for the detection of e.g., pressure [18–20], temperature [21], and sound [22, 23]. These structures are highly sensitive and integrated, especially in [18, 19], and the cross-axial configuration that the FP cavity is on the side of the fiber instead of the end of the fiber exhibits a great advantage in measuring static pressure of fluid. However, they tend to be complex to fabricate due to the necessity of external reflective surfaces. The structure of all-fiber with simple fabrication and compact structure is obviously more promising in temperature sensing [24–26]. In 2016, Yin et al. proposed a two-step polishing technique to fabricate an assembly-Free-Based Fiber-Optic MI for the first time and did preliminary study on high temperature sensing [25], without involving the study of reproduction and other properties. In 2020, an all-fiber FP interferometer based on an angled fiber sensor, which realizes temperature sensing through interference between light reflected directly back to the fiber core and light first reflected to the cladding and subsequently coupled into the fiber core, was proposed by Zhang et al. [24], which has advantages of ease of fabrication and all-fiber characteristics. However, similar to other traditional FP sensors, the optical path difference (OPD) and temperature sensitivity of this interference structure are both affected by the machining error, which results in low reproducibility. Moreover, such SMF based tip polished sensors will be greatly influenced by the coupling effect of two orthogonal polarization states of fundamental mode in lead-in SMF, which make the interference spectrum unstable when lead-in SMF suffers from bending, pressing, or twisting.

With the purpose of realizing the benefits of such devices while not suffering from the fabrication and polarization dependence drawbacks of previous designs, in this paper, we mainly focus on developing and experimentally studying a reproducible and stable fiber tip MI based on polarization maintaining fiber (PMF). Compared to the previous work reported by Yin et al. [25], the angled PMF tip is fabricated by only using a one-step partial-polishing technique, which is an effective method to control both the oblique angle and polishing depth. Experimental studies show that the OPD between the beams is consistent across different samples, which ensures fabrication repeatability. Furthermore, the interference spectrum keeps stable when the lead-in PMF suffers from bending, twisting, and even shaking. As for the application of high temperature sensing, the all-fiber structure ensures the reproducibility and stability of the sensor in high temperature environment, and the anneal effect is also found in this research. In addition, compared to most of the MZ based high-temperature sensors [10, 27, 28], the proposed fiber tip MI operates in a reflection mode of detection, which is more convenient for practically high spatial detection.

2. OPERATING PRINCIPLE AND FABRICATION

2.1. Operating Principle

Figures 1(a) and (b) show the cross section and a structure schematic of the proposed PMF tip MI, where half of the tip (core and cladding) is polished to 45° , and the polished plane is parallel to the slow axis of PMF. For p -polarized input light, it will be split into two perpendicular beams, E_{1-p} and E_{2-p} , with a splitting factor $\gamma_p = E_{1-p}/(E_{1-p} + E_{2-p})$ that is dependent on the polishing depth. The light reflected by the oblique part of the fiber tip core, E_{2-p} , is normally incident on the cladding side surface and reflected back to the core where it recombines with E_{1-p} , with resulting interference. Assuming that the p -polarized light amplitude of the electrical field launched into the fiber is E_{0-p} , the output

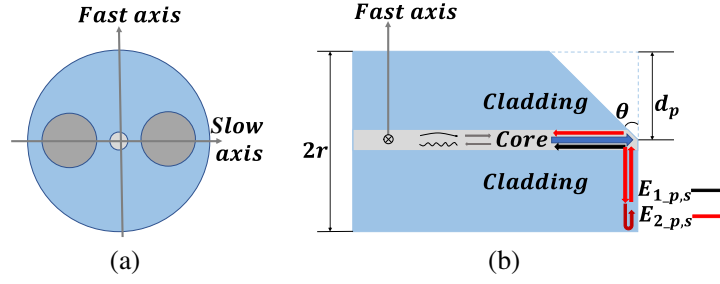


Figure 1. (a) The schematic cross section of PMF. (b) Configuration of the polished PMF tip MI.

intensity of p-light is:

$$I_{out-p} = (E_{0-p} \cdot \gamma_p)^2 \cdot R_{co-0-p} + [E_{0-p} \cdot (1 - \gamma_p)]^2 \cdot R_{co-45-p}^2 \cdot R_{cl-0-p} \cdot \alpha_p + 2 \cdot E_{0-p}^2 \cdot \gamma_p \cdot (1 - \gamma_p) \cdot R_{co-45-p} \cdot \sqrt{R_{co-0-p} \cdot R_{cl-0-p} \cdot \alpha_p} \cdot \cos(\varphi_p) \quad (1)$$

where R_{co-0-p} and R_{cl-0-p} are the p-light reflectivity at the normal part of the core end face and the cladding side surface; $R_{co-45-p}$ is the p-light reflectivity at the oblique part of the core end face; α_p is the coupling coefficient of the p-light reflected beam in the cladding into the core, which is mainly dependent on the oblique angle and flatness of the polished surface. φ_p is the phase difference between the two p-polarized reflected beams.

$$\varphi_p = 2\pi\xi/\lambda + 2\Delta\varphi_p + \varphi_{0-p} \quad (2)$$

λ is the wavelength ξ ; $\Delta\varphi_p$ and φ_{0-p} is the OPD, the phase change of Fresnel reflection and initial phase difference between the two p-polarized reflected beams, respectively. Similarly, for s-polarized input light, the output intensity and the phase difference of s-light can be expressed as:

$$I_{out-s} = (E_{0-s} \cdot \gamma_s)^2 \cdot R_{co-0-s} + [E_{0-s} \cdot (1 - \gamma_s)]^2 \cdot R_{co-45-s}^2 \cdot R_{cl-0-s} \cdot \alpha_s + 2 \cdot E_{0-s}^2 \cdot \gamma_s \cdot (1 - \gamma_s) \cdot R_{co-45-s} \cdot \sqrt{R_{co-0-s} \cdot R_{cl-0-s} \cdot \alpha_s} \cdot \cos(\varphi_s) \quad (3)$$

$$\varphi_s = 2\pi\xi/\lambda + 2\Delta\varphi_s + \varphi_{0-s} \quad (4)$$

It should be noticed that the initial input electrical amplitude, reflectivity at the end-face, and the phase change induced by Fresnel reflection are different between p-polarized and s-polarized light. Therefore, the total output is the superimposed interference spectrum of the two orthogonal polarization states. Due to the slight birefringence difference in SMF, two orthogonal polarization states will couple to each other easily when SMF is disturbed, namely the composite output spectrum is unstable. Fortunately, PMF with large birefringence can maintain the polarization of probe light. Once the polarization of input light is determined, the output interferometric spectrum keeps stable even PMF suffers from disturbance, such as bending or twisting.

For simplifying the analysis, considering that the core of SMF is in the center of the fiber and ignoring the RI difference between the core and the cladding, the optical path difference ξ can be expressed as $2nL$, where n is the RI of the fiber cladding, and L is the distance from core oblique end face to the cladding side surface that is equal to fiber radius r .

Considering the negligible RI difference between the core and cladding of the SMF, we can reasonably assume $R_{co-0-p} = R_{cl-0-p}$ and $R_{co-0-s} = R_{cl-0-s}$, and we denote $R_{fiber-air-p}$ and $R_{fiber-air-s}$ in the following for p-light and s-light, respectively. The RI of the core is about 1.4681 (Nufern, USA, PM1550-XP), and due to the characteristics of total reflection, $R_{co-45-p} = 1$. From Eq. (1) we thus find the reflected spectrum of p-light and s-light and the superimposed reflected spectrum to be:

$$R_p = I_{out-p}/I_{in-p} = (\gamma_p)^2 \cdot R_{fiber-air-p} + (1 - \gamma_p)^2 \cdot R_{fiber-air-p} \cdot \alpha_p + 2 \cdot \gamma_p \cdot (1 - \gamma_p) \cdot R_{fiber-air-p} \cdot \sqrt{\alpha_p} \cdot \cos(2\pi\xi/\lambda + 2 \cdot \Delta\varphi_p + \varphi_{0-p}) = A_p + B_p \cdot \cos(2\pi\xi/\lambda + \delta_p) \quad (5)$$

$$R_s = I_{out-s}/I_{in-s} = (\gamma_s)^2 \cdot R_{fiber-air-s} + (1 - \gamma_s)^2 \cdot R_{fiber-air-s} \cdot \alpha_s + 2 \cdot \gamma_s \cdot (1 - \gamma_s) \cdot R_{fiber-air-s} \cdot \sqrt{\alpha_s} \cdot \cos(2\pi\xi/\lambda_s + 2 \cdot \Delta\varphi_s + \varphi_{0-s}) = A_s + B_s \cdot \cos(2\pi\xi/\lambda + \delta_s) \quad (6)$$

$$\begin{aligned} R_{total} &= R_p + R_s = A_p + A_s + B_p \cdot \cos(2\pi\xi/\lambda + \delta_s) + B_s \cdot \cos(2\pi\xi/\lambda + \delta_s) \\ &= A_{total} + B_{total} \cdot \cos(2\pi\xi/\lambda + \delta_{total}) \end{aligned} \quad (7)$$

where B_{total} and δ_{total} are the amplitude and phase of superimposed reflected spectrum, which can be expressed as:

$$B_{total} = \sqrt{B_p^2 + B_s^2 + 2B_p B_s \cos(\delta_p - \delta_s)} \quad (8)$$

$$\delta_{total} = \arctan [(B_p \sin \delta_p + B_s \sin \delta_s) / (B_p \cos \delta_p + B_s \cos \delta_s)] \quad (9)$$

Eqs. (8) and (9) show that the amplitude and phase of the superimposed reflected spectrum are both relative to the amplitude and phase of p-light and s-light spectrum, namely strong determined by the initial polarization state of the input light.

When the phase term satisfies the condition $4\pi nL/\lambda + \varphi = (2m + 1)\pi$, where m is an integer, we find a reflectivity minimum at resonant wavelengths of p-light and s-light which are:

$$\lambda_{dip-p} = 4\pi nL / [(2m + 1)\pi - (\Delta\varphi_p + \varphi_{0-p})] \quad (10)$$

$$\lambda_{dip-s} = 4\pi nL / [(2m + 1)\pi - (\Delta\varphi_s + \varphi_{0-s})] \quad (11)$$

Eqs. (10) and (11) show that the resonant wavelengths of p-light and s-light in the interference spectrum are different because of the different phase changes induced by Fresnel reflection and are both proportional to the RI and radius of cladding. As evident from Eqs. (10) and (11), the spectrum will drift as the temperature changes, and the temperature sensitivities of p-light and s-light can be expressed as [29]:

$$\Delta\lambda_{dip-p} / \Delta T = \lambda_{dip-p} \cdot [\Delta n/n \cdot \Delta T + \Delta L / (L \cdot \Delta T)] = \lambda_{dip-p} \cdot (\kappa/n + \sigma) \quad (12)$$

$$\Delta\lambda_{dip-s} / \Delta T = \lambda_{dip-s} \cdot [\Delta n/n \cdot \Delta T + \Delta L / (L \cdot \Delta T)] = \lambda_{dip-s} \cdot (\kappa/n + \sigma) \quad (13)$$

where Δn and ΔL are the variation of fiber cladding RI and cladding radius L caused by temperature change. κ is the thermo-optic coefficient of silica, $\sim 1.28 \times 10^{-5}/^\circ\text{C}$ [30], and σ is the thermal expansion coefficient of silica, $\sim 5.5 \times 10^{-7}/^\circ\text{C}$ [31]. The temperature sensitivities are different since the resonant wavelengths of p-light and s-light are slightly different. By substituting the above parameters into the formula (9) or (10), the theoretical temperature sensitivity of the structure can be calculated as about 14.4 pm/ $^\circ\text{C}$ at 1550 nm.

2.2. Fabrication

Figure 2 illustrates the fabrication of the PMF MI tip. An optical fiber end face polishing machine, shown in Figure 2(a), with the ability to polish optical fibers at selectable and variable angles with an angle tolerance of $\pm 1.5^\circ$ and a depth tolerance of $\pm 3 \mu\text{m}$, was fabricated in-house. To obtain a PMF tip MI with a suitable fringe visibility, the oblique angle and polishing depth are preliminarily designed to be 45° and $62.5 \mu\text{m}$, respectively. A cleaved PMF is fastened in a fiber clamp with an adjustable oblique angle, and the fiber tip is adjusted to connect with the polishing pan at a designed angle of 45° . A microscope is used to observe the fiber tip, and a spectrometer is used to monitor the reflection of the fiber to estimate the polishing depth. Diamond sandpaper with roughness of 4000 mesh is used for polishing optical fiber end face. In this experiment, the polished plane is parallel to the slow axis of PMF. The spectrometer continuously scans the spectrum in the range 1500 nm to 1600 nm with a resolution of 0.5 nm, and the interference spectrum with periodic fluctuation appearing in the spectrum indicates that the polishing plane has reached the fiber core. Figure 2(b) shows the fabricated PMF tip MI, and the inset is the microscope image of polished cross section of PMF tip.

3. CHARACTERIZATION AND EXPERIMENT VERIFICATION

3.1. Influence of Polarization

To study the influence of the input light polarization, we prepared angled fiber samples of SMF and PMF with oblique angles of $\sim 45^\circ$, all having the same polishing depth of $62 \pm 3 \mu\text{m}$. First, different polarization states of input laser source are randomly set by controlling the fiber polarization controller.

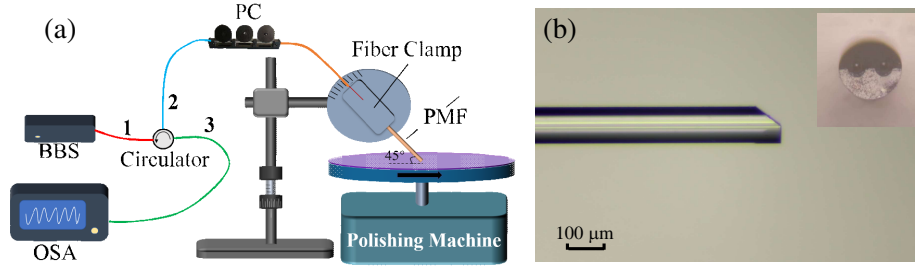


Figure 2. Configuration of a PMF tip MI. (a) Setup of the fiber tip polishing process. (b) Micrograph of the fiber tip MI. Inset in Figure 2 (b): the microscope image of polished cross section.

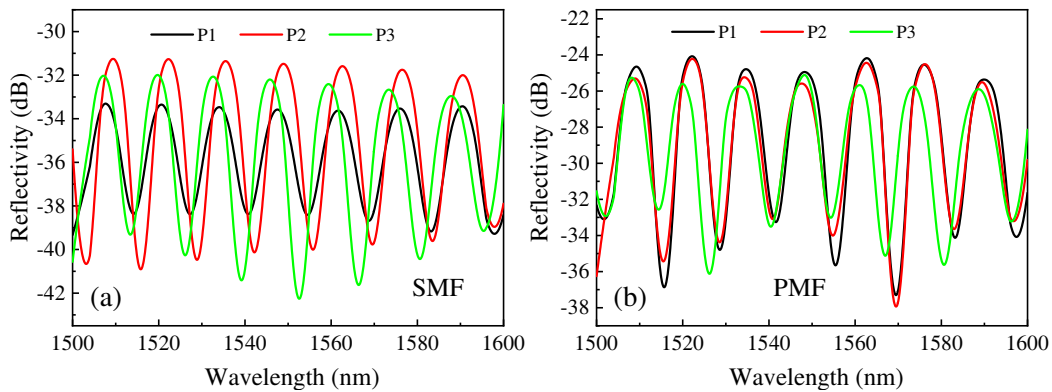


Figure 3. The reflected spectrums of (a) SMF and (b) PMF tip MI samples with different input light polarization.

The reflected spectrums of SMF and PMF tip MI samples with different input light polarizations are recorded and shown in Figures 3(a) and (b). Experimental results verify that the composite interference spectrums of SMF based and PMF based tip MIs are both affected by the initial input light polarization, which is consistent with the theoretical analysis.

In addition, lead-in fiber sections of SMF tip MI and PMF tip MI samples are fixed on two parallel moving stages successively, and different bending radii can be adjusted by moving one of the stages. Figures 4(a) and (b) show the reflected spectrums of SMF and PMF tip MI samples with and without bending the lead-in fiber section, respectively. Then, lead-in fiber sections of these two types of samples are installed in a rotated fiber clamp to twist the fiber. Figures 4(c) and (d) represent the reflected spectrums of SMF and PMF tip MI samples with and without twisting the lead-in fiber section. It can be clearly seen that SMF based sample is obviously influenced by bending or twisting, while PMF based sample is not. Experimental results show that the PMF based tip MI sensor has excellent stability even with lead-in PMF section suffering from mechanical disturbance.

3.2. Reproduction Capacity

To estimate the reproducibility of the PMF tip MI, we prepared several samples successively with the same process, and the polishing angles and polishing depths of these samples were $45 \pm 1.5^\circ$ and $62 \pm 3 \mu\text{m}$, respectively. The reflection spectra were measured in the range 1300–1630 nm, and the input polarization keeps the same during the measurement. The purpose of expanding the spectral width was to obtain sufficient spectral data to improve the calculation accuracy of L . According to Eqs. (5) and (6), the $R-\lambda$ spectra of the interferometers that represent the variation of reflectivity with wavelength are not strictly periodic; however, the $R-1/\lambda$ spectra that represent the variation of reflectivity with inverse wavelength are periodic as the independent variable is $1/\lambda$, and the period is $1/2nL$ theoretically.

Using the spectral data, with the wavelength replaced with its inverse, the $R-1/\lambda$ spectra of the

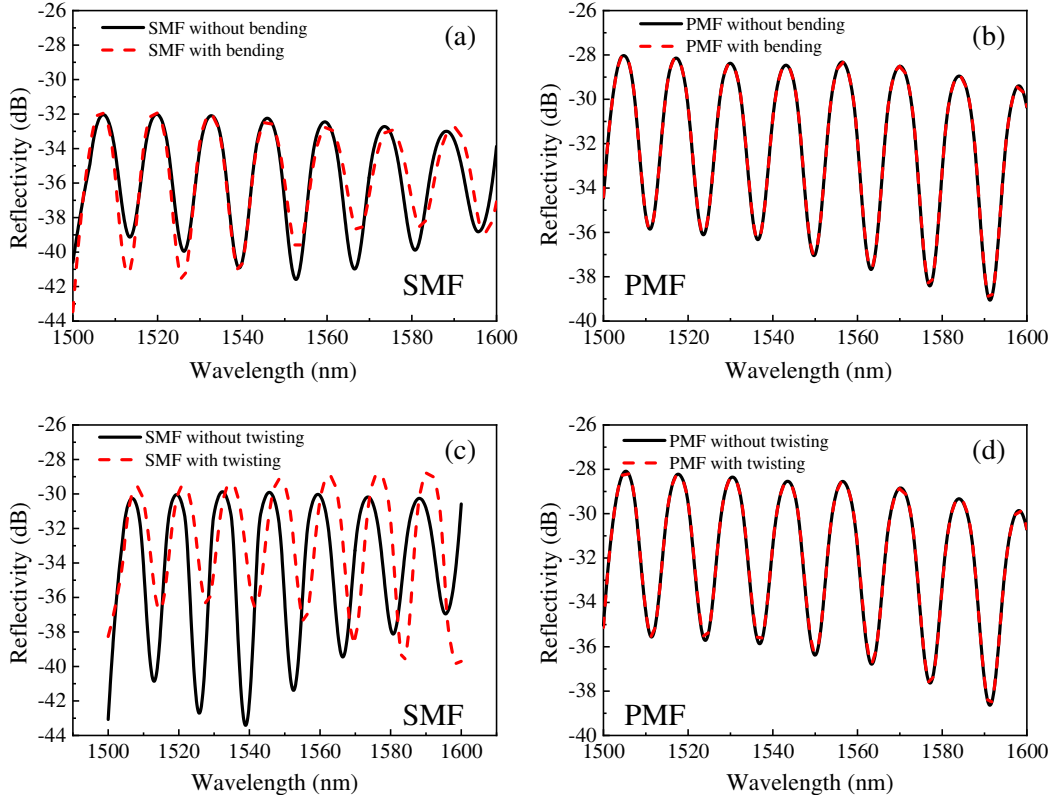


Figure 4. The reflected spectrums of (a) SMF and (b) PMF tip MI samples with and without bending the lead-in fiber section. The reflected spectrums of (c) SMF and (d) PMF tip MI samples with and without twisting the lead-in fiber section.

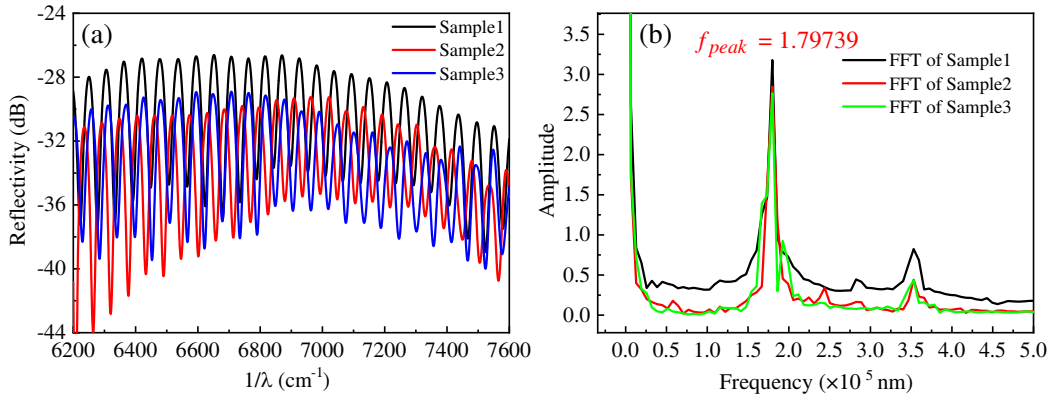


Figure 5. (a) Reflectivity varies with $1/\lambda$ of three samples with λ in the range 1300–1630 nm. (b) FFT spectra of the spectra shown in (a).

three samples, shown in Figure 5(a), were obtained by resampling of the $R-1/\lambda$ data. The OPD of the interferometer, $2nL$, can be calculated directly by a Fourier transformation of the $R-1/\lambda$ spectra according to Eqs. (5) and (6). The Fourier transform curves are shown in Figure 5(b), and as can be seen from the figure, the frequency peaks of three samples are $179.739 \mu\text{m}$ with a frequency resolution of $6.421 \mu\text{m}$. L can be calculated by:

$$L = f_{peak}/2n \quad (14)$$

where n is the RI of fiber cladding, which is about 1.4628 (Nufern, USA, PM1550-XP), and f_{peak} is

the peak frequency of the $R-1/\lambda$ spectra Fourier transform curves. The calculated result is that L , the distance from core oblique end face to the cladding side surface, of all three samples is about $61.4 \mu\text{m}$, that is nearly equal to the fiber radius $62.5 \mu\text{m}$. The result shows that the PMF tip MI we proposed has a fixed OPD that is not affected by processing error, i.e., the proposed fiber tip MI is reproducible.

3.3. High-Temperature Sensing

To verify the high temperature response of the PMF tip MI, we experimentally tested the temperature responses of three samples with polishing angle of $45 \pm 1.5^\circ$ and polishing depth of $62 \pm 3 \mu\text{m}$ prepared with the same process (45° and $62 \mu\text{m}$ are the design parameters, and $\pm 1.5^\circ$ and $\pm 3 \mu\text{m}$ are process errors, respectively). The PMF tip MI is placed into tubular oven that has a temperature range from 50°C to 1200°C , and a thermocouple is used for temperature measurement near the MI probe, as shown in Figure 6. The temperature performance was characterized by tracking the dips near 1550 nm in the reflection spectra of the three samples. Figures 7(a), (c), and (e) show the reflection spectra of the PMF tip MI at different temperatures, and we find that the spectra are linearly red-shifted with increasing temperature.

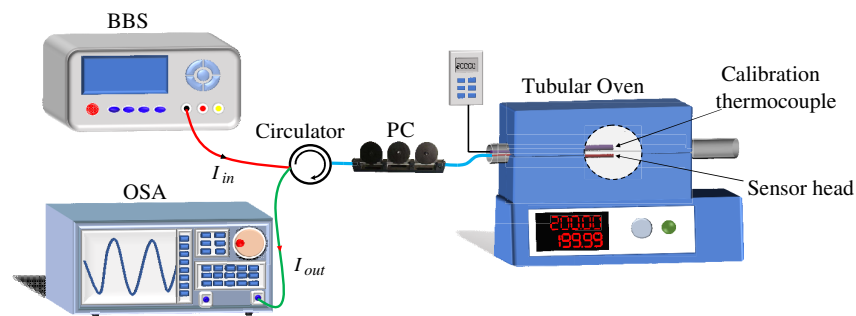


Figure 6. Schematic of the experimental setup.

Prior to temperature calibration, the sensors were annealed for half an hour at 1000°C . Figures 7(a) and (b) show the different temperature response spectrums and linear fitting results of Sample 1 before and after annealing, indicating that the annealing treatment can release residual stress in the fiber, which is of importance to ensure the reliability and reversibility of the fiber temperature probe. The wavelength shifts of the resonant dip around 1550 nm of Sample 1 during additional heating and cooling in the range of 100°C to 1000°C are also performed. It can be seen that the temperature response of Sample 1 has a good linearity ($R^2 = 0.9964$) after annealing, and the measured results of heating and cooling process are in good agreement that indicates the reversibility for high-temperature sensing. For comparison, resonant wavelength shifts nearest to 1550 nm of Samples 2 and 3 after annealing is plotted in Figures 7(c)–(d) and (e)–(f), respectively. In both cases, the results show that the temperature responses of heating and cooling have a good coincidence, and the relationship between the wavelength shift and temperature change is highly linear. We find the temperature sensitivities of the three samples to be $14.93 \text{ pm}/^\circ\text{C}$, $15.54 \text{ pm}/^\circ\text{C}$, and $14.99 \text{ pm}/^\circ\text{C}$, which are consistent well with the theoretical value of $14.4 \text{ pm}/^\circ\text{C}$. The difference between measured and theoretical values may be caused by the deviation of practical thermal expansion coefficient, thermo-optic coefficient, and the RI of silica. The difference between the sensitivities of the samples and their average sensitivity of $15.15 \text{ pm}/^\circ\text{C}$ is less than 4.0%, again demonstrating the reproducibility of the PMF tip MI.

A comparison of the sensor structure, sensitivity, linear range, detection mode, and fabrication of the various typical high temperature sensors reported in the previous work done in recent years and this work is presented in Table 1. The sensitivity of the proposed high temperature sensor is at the same level as that of most types of high temperature sensors, which are mainly determined by the properties of silica material. High temperature sensor based on MZI has always shown high temperature sensitivity, and it is often accompanied by transmission detection mode and complex preparation process, which leads to the lack of compactness. Similar to the fabrication of fusing splicing fiber, the fabrication of

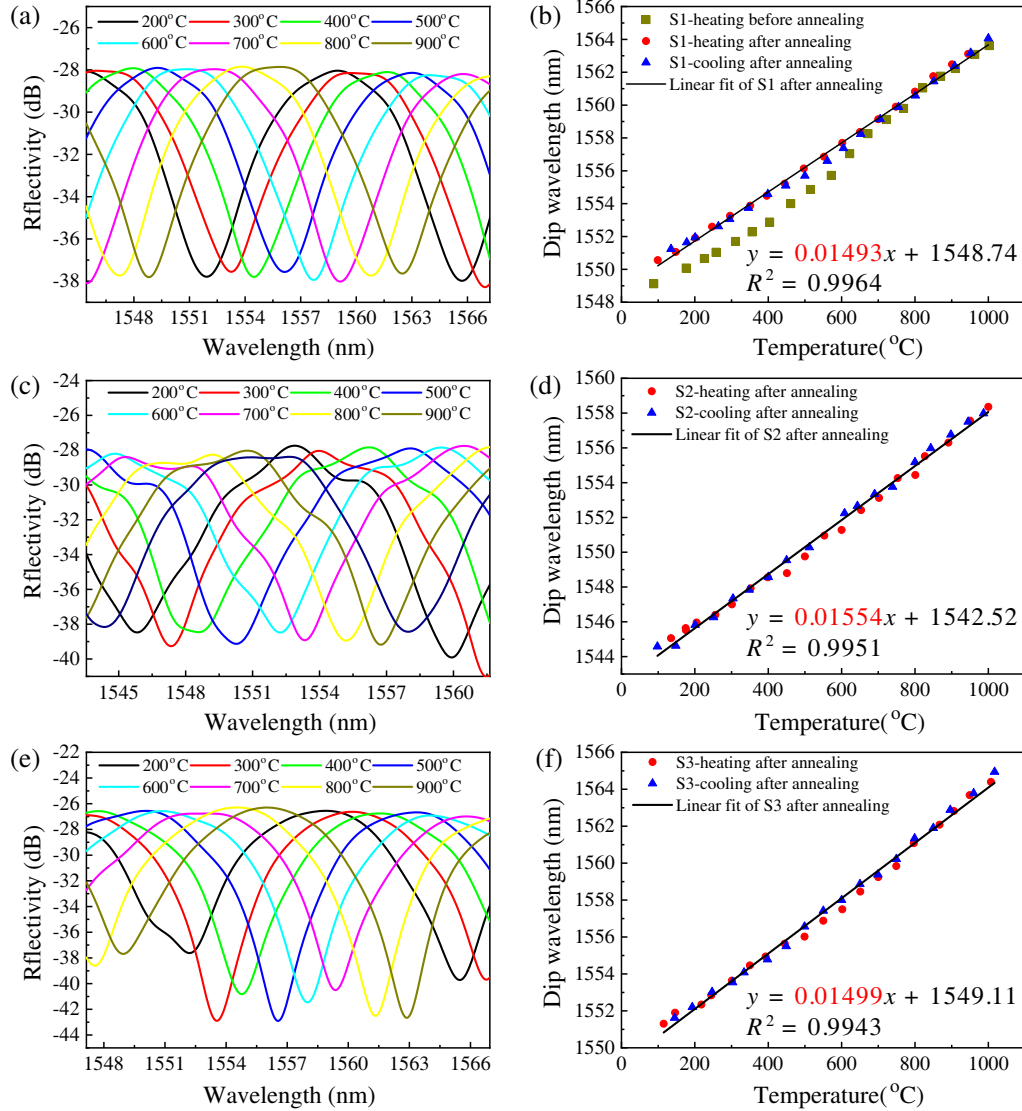


Figure 7. Measured temperature spectral response of (a) Sample 1, (c) Sample 2, and (e) Sample 3. Wavelength shift of the dip as a function of temperature during heating and cooling processes in (b) Sample 1, (d) Sample 2 and, (e) Sample 3. The first heating scatter plot in (b) shows the temperature response of Sample 1 before annealing.

Table 1. Characteristics comparison of some typical high temperature optical fiber sensors.

Reference	Sensor Structure	Sensitivity (pm/°)	Linear Range (°)	Sensing length along fiber direction	Fabrication	Reproducibility
[7]	Tip packaged FPI	12.51	50–800	~ 81.7 μm	Fusing splicing	Average
[12]	Sapphire FPI	13.57	20–1000	~ 600 μm	Fusing splicing	Average
[28]	MZI	87	30–1000	~ 8 mm	Tapering	Average
[32]	Tilted FBG	15.72	Up to 800	~ 5 mm	Femtosecond laser	Good
[33]	HC-PCF	15.68	200–1200	~ 1–4 mm	Fusing splicing	Average
This work	Tip MI	15.15	100–1000	A few μm	One-step Polishing	Good

tapering will greatly reduce the mechanical strength, vibration resistance, and stability of the sensor structure, and these preparation processes are often difficult to control and achieve repeated production. Compared with other types of high temperature optical fiber sensors, the proposed PMF tip MI has a compact and stable structure formed by a single one-step polishing process and can achieve repeated production, low cost, and especially immune to mechanical disturbances.

4. CONCLUSION

A highly compact and reproducible all-fiber tip Michelson interferometer based on polarization maintaining fiber was developed and experimentally demonstrated. This structure is easily fabricated by only partial polishing of the fiber end face once. The influence of polarization and the reproducibility of the structure were investigated theoretically and experimentally. Sample high-temperature measurements were carried out, and the temperature sensitivities of 14.93 pm/°C, 15.54 pm/°C, and 14.99 pm/°C were obtained for three samples after annealing treatment. The difference between the sensitivities of these tested samples is less than 4.0%. Being easily fabricated, having good reproducibility and excellent performance of mechanical stability, the proposed PMF base tip Michelson interferometer has good prospects for mass-produced fiber high temperature sensors with high spatial resolution.

ACKNOWLEDGMENT

This work was supported partially by the China Postdoctoral Science Foundation (No. 2018M642423) the National Key Research and Development Program of China (No. 2018YFC1407503), the Key Research and Development Program of Zhejiang Province (2021C03178), the Ningbo Science and Technology Project (20211ZDYF020243), Shanghai Zhangjiang Science City special development fund, and Ningbo Science and Technology Plan Project-Key Core Technology Emergency Tackling Plan Project (2020G012).

DISCLOSURES

The authors declare that there are no conflicts of interest related to this article.

REFERENCES

1. Lee, B. H., Y. H. Kim, K. S. Park, J. B. Eom, M. J. Kim, B. S. Rho, and H. Y. Choi, "Interferometric fiber optic sensors," *Sensors*, Vol. 12, 2467–2486, 2012.
2. Wu, S., G. Yan, B. Zhou, E. Lee, and S. He, "Open-cavity Fabry-Perot interferometer based on etched side-hole fiber for microfluidic sensing," *IEEE Photonics Technology Letters*, Vol. 27, 1813–1816, 2015.
3. Abbas, L. G. and H. Li, "Temperature sensing by hybrid interferometer based on Vernier like effect," *Optical Fiber Technology*, Vol. 64, 102538, 2021.
4. Wang, T., M. Wang, and H. Ni, "Micro-Fabry-Pérot interferometer with high contrast based on an in-fiber ellipsoidal cavity," *IEEE Photonics Technology Letters*, Vol. 24, 948–950, 2012.
5. Favero, F. C., G. Bouwmans, V. Finazzi, J. Villatoro, and V. Pruneri, "Fabry-Perot interferometers built by photonic crystal fiber pressurization during fusion splicing," *Optics Letters*, Vol. 36, 4191–4193, 2011.
6. Liu, X., M. Jiang, Q. Sui, and X. Geng, "Optical fibre Fabry-Perot relative humidity sensor based on HCPCF and chitosan film," *Journal of Modern Optics*, Vol. 63, 1668–1674, 2016.
7. Su, H., Y. Zhang, K. Ma, Y. Zhao, and C. Yu, "Tip packaged high-temperature miniature sensor based on suspended core optical fiber," *Journal of Lightwave Technology*, Vol. 38, 4160–4165, 2020.

8. Ferreira, M. S., L. Coelho, K. Schuster, J. Kobelke, and J. L. Santos, and O. Frazão, “Fabry-Perot cavity based on a diaphragm-free hollow-core silica tube,” *Optics Letters*, Vol. 36, 4029–4031, 2011.
9. Zhang, Z., J. He, B. Du, F. Zhang, K. Guo, and Y. Wang, “Measurement of high pressure and high temperature using a dual-cavity Fabry-Perot interferometer created in cascade hollow-core fibers,” *Optics Letters*, Vol. 43, 6009–6012, 2018.
10. Choi, H. Y., K. S. Pack, S. J. Park, U. Paek, B. H. Lee, and E. S. Choi, “Miniature fiber-optic high temperature sensor based on a hybrid structured Fabry-Perot interferometer,” *Optics Letters*, Vol. 33, 2455–2457, 2008.
11. Lee, D., M. Yang, C. Huang, and J. Dai, “Optical fiber high-temperature sensor based on dielectric films extrinsic Fabry-Pérot cavity,” *IEEE Photonics Technology Letters*, Vol. 26, 2107–2110, 2014.
12. Yu, X., S. Wang, J. Jiang, et al., “Hybrid sapphire dual-Fabry-Perot-cavities sensor for high temperature and RI measurement,” *Journal of Lightwave Technology*, Vol. 39, 3911–3918, 2021.
13. Zhang, H., Z. Wu, P. P. Shum, et al., “Highly sensitive strain sensor based on helical structure combined with Mach-Zehnder interferometer in multicore fiber,” *Scientific Reports*, Vol. 7, 46633–46633, 2017.
14. Wei, T., Y. Han, H. Tsai, and H. Xiao, “Miniaturized fiber inline Fabry-Perot interferometer fabricated with a femtosecond laser,” *Optics Letters*, Vol. 33, 536–538, 2008.
15. Chen, P. and X. Shu, “Refractive-index-modified-dot Fabry-Perot fiber probe fabricated by femtosecond laser for high-temperature sensing,” *Optics Express*, Vol. 26, 5292–5299, 2018.
16. Gao, H., Y. Jiang, Y. Cui, L. Zhang, J. Jia, and L. Jiang, “Investigation on the thermo-optic coefficient of silica fiber within a wide temperature range,” *Journal of Lightwave Technology*, Vol. 36, 5881–5886, 2018.
17. Liao, C. R., D. N. Wang, M. Wang, and M. Yang, “Fiber in-line Michelson interferometer tip sensor fabricated by femtosecond laser,” *IEEE Photonics Technology Letters*, Vol. 24, 2060–2063, 2012.
18. Bae, H., X. M. Zhang, H. Liu, and M. Yu, “Miniature surface-mountable Fabry-Perot pressure sensor constructed with a 45° angled fiber,” *Optics Letters*, Vol. 35, 1701–1703, 2010.
19. Bae, H., L. Dunlap, J. Wong, and M. Yu, “Miniature temperature compensated fabry-perot pressure sensors created with self-aligned polymer photolithography process,” *IEEE Sensors Journal*, Vol. 12, 1566–1573, 2012.
20. Zhu, J., M. Wang, L. Chen, X. Ni, and H. Ni, “An optical fiber Fabry-Perot pressure sensor using corrugated diaphragm and angle polished fiber,” *Optical Fiber Technology*, Vol. 34, 42–46, 2017.
21. Pang, C., H. Bae, A. Gupta, K. Bryden, and M. Yu, “MEMS Fabry-Perot sensor interrogated by optical system-on-a-chip for simultaneous pressure and temperature sensing,” *Optics Express*, Vol. 21, 21829–21839, 2013.
22. Wang, W., N. Wu, Y. Tian, X. Wang, C. Niezrecki, and J. Chen, “Optical pressure/acoustic sensor with precise Fabry-Perot cavity length control using angle polished fiber,” *Optics Express*, Vol. 17, 16613–16618, 2009.
23. Liu, B., J. Lin, J. Wang, C. Ye, and P. Jin, “MEMS-based high-sensitivity Fabry-Perot acoustic sensor with a 45° angled fiber,” *IEEE Photonics Technology Letters*, Vol. 28, 581–584, 2016.
24. Zhang, X., L. Li, X. Zou, et al., “Angled fiber-based Fabry-Perot interferometer,” *Optics Letters*, Vol. 45, 292–295, 2020.
25. Yin, J., T. Liu, J. Jiang, et al., “Assembly-free-based fiber-optic micro-michelson interferometer for high temperature sensing,” *IEEE Photonics Technology Letters*, Vol. 28, 625–628, 2016.
26. Wang, T., K. Liu, J. Jiang, M. Xue, P. Chang, and T. Liu, “A large range temperature sensor based on an angled fiber end,” *Optical Fiber Technology*, Vol. 45, 19–23, 2018.
27. Jiang, L., J. Yang, S. Wang, B. Li, and M. Wang, “Fiber Mach-Zehnder interferometer based on microcavities for high-temperature sensing with high sensitivity,” *Optics Letters*, Vol. 36, 3753–3755, 2011.
28. Zhao, N., Q. Lin, W. Jing, et al., “High temperature high sensitivity Mach-Zehnder interferometer based on waist-enlarged fiber bitapers,” *Sensors and Actuators A: Physical*, Vol. 267, 491–495, 2017.

29. Li, Z., J. Tian, Y. Jiao, Y. Sun, and Y. Yao, "Simultaneous measurement of air pressure and temperature using fiber-optic cascaded Fabry-Perot interferometer," *IEEE Photonics Journal*, Vol. 11, 1–10, 2019.
30. Tian, J., Y. Jiao, S. Ji, X. Dong, and Y. Yao, "Cascaded-cavity Fabry-Perot interferometer for simultaneous measurement of temperature and strain with cross-sensitivity compensation," *Optics Communications*, Vol. 412, 121–126, 2018.
31. Wu, Y., Y. Zhang, J. Wu, and P. Yuan, "Fiber-optic hybrid-structured Fabry-Perot interferometer based on large lateral offset splicing for simultaneous measurement of strain and temperature," *Journal of Lightwave Technology*, Vol. 35, 4311–4315, 2017.
32. Wang, R., J. Si, T. Chen, et al., "Fabrication of high-temperature tilted fiber Bragg gratings using a femtosecond laser," *Optics Express*, Vol. 25, 23684–23689, 2017.
33. Lei, X. and X. Dong, "High-sensitivity Fabry-Perot interferometer high-temperature fiber sensor based on vernier effect," *IEEE Sensors Journal*, Vol. 20, 5292–5297, 2020.